JACS
JOURNAL OF THE AMERICAN CHEMICAL SOCIETY
Article
pubs.acs.org/JACS

Insight into Strain Effects on Band Alignment Shifts, Carrier Localization and Recombination Kinetics in CdTe/CdS Core/Shell Quantum Dots

Lihong Jing,[†,∥] Stephen V. Kershaw,[‡,∥] Tobias Kipp,[§,∥] Sergii Kalytchuk,[‡] Ke Ding,[†] Jianfeng Zeng,[†] Mingxia Jiao,[†] Xiaoyu Sun,[†] Alf Mews,[§] Andrey L. Rogach,[‡] and Mingyuan Gao*[,†]

[†]Institute of Chemistry, Chinese Academy of Sciences, Bei Yi Jie 2, Zhong Guan Cun, Beijing 100190, China

[‡]Department of Physics and Materials Science & Centre for Functional Photonics, City University of Hong Kong, Tat Chee Avenue, Kowloon, Hong Kong

[§]Institute of Physical Chemistry, University of Hamburg, Grindelallee 117, 20146 Hamburg, Germany

Supporting Information

ABSTRACT: The impact of strain on the optical properties of semiconductor quantum dots (QDs) is fundamentally important while still awaiting detailed investigation. CdTe/CdS core/shell QDs represent a typical strained system due to the substantial lattice mismatch between CdTe and CdS. To probe the strain-related effects, aqueous CdTe/CdS QDs were synthesized by coating different sized CdTe QD cores with CdS shells upon the thermal decomposition of glutathione as a sulfur source under reflux. The shell growth was carefully monitored by both steady-state absorption and fluorescence spectroscopy and transient fluorescence spectroscopy. In combination with structural analysis, the band alignments as a consequence of the strain were modified based on band deformation potential theory. By further taking account of these strain-induced band shifts, the effective mass approximation (EMA) model was modified to simulate the electronic structure, carrier spatial localization, and electron–hole wave function overlap for comparing with experimentally derived results. In particular, the electron/hole eigen energies were predicted for a range of structures with different CdTe core sizes and different CdS shell thicknesses. The overlap of electron and hole wave functions was further simulated to reveal the impact of strain on the electron–hole recombination kinetics as the electron wave function progressively shifts into the CdS shell region while the hole wave function remains heavily localized in CdTe core upon the shell growth. The excellent agreement between the strain-modified EMA model with the experimental data suggests that strain exhibits remarkable effects on the optical properties of mismatched core/shell QDs by altering the electronic structure of the system.

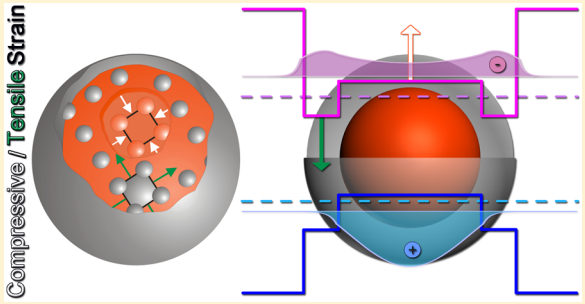

INTRODUCTION

Fluorescent semiconductor quantum dots (QDs) have shown great potentials for lighting, display, and solar energy harvesting in the optoelectronic field,[1−6] as well as sensing and imaging in the biomedical field.[7−9] However, to fully bridge the gap between potential and actual commercial grade performance, in many cases a deeper and more detailed understanding of the underlying mechanisms behind the optical properties of QDs is needed to fully meet the requirements of these applications.

Construction of semiconductor/semiconductor core/shell structures has been demonstrated to be one of the most effective ways to improve the photoluminescence (PL) efficiency and tune the PL emission of QDs as well.[10−16] According to the band offset between core and shell, core/shell QDs can generally be classified as type I and type II structures. In type I structures, the bandgap of the core is narrow and lies within the bandgap of the shell, which is favorable for improving the PL quantum yield (QY),[10,12] because the photogenerated electrons and holes are confined within the particle core. In type II QDs, the conduction and valence bands of core and shell are staggered. By manipulating their relative positions, the PL emission can often be tuned over a large wavelength range.[17,18] Moreover, the photogenerated electrons and holes are spatially segregated in type II structures, being preferentially confined with one charge carrier in the core and the counterpart carrier in the shell.[17,19−21] The reduced overlap of wave functions of electrons and holes consequently decreases the radiative recombination rate of the exciton. Per se, in the absence of nonradiative recombination, this reduced recombination rate would not affect the PL QY. However, when radiative and nonradiative processes are both present, the ratio of their rates critically affects the benefit of the type II heterostructure in terms of the PL QY. Apart from the classic type I and type II core/shell structures, reverse type I, core/shell/shell structures, and even more complicated combinations

Received: December 15, 2014
Published: January 16, 2015

DOI: 10.1021/ja5127352
J. Am. Chem. Soc. 2015, 137, 2073−2084

of type I and type II structures have been explored to tune the optical properties of QDs.[22,23]

However, the formation of core/shell QD heterostructures often involves lattice mismatch at the interface between two crystalline materials with different lattice parameters. On the bulk length scale, lattice mismatch can often be gradually accommodated using alloys or thin superlattices to ease the transition between the two materials. On the nanometer scale, the whole QD is typically as small as 3−10 nm and the shell itself may only be a few atomic layers in thickness; therefore, additional strain relief layers may not be an option. There are only a few exceptions among the binary combinations of semiconductor materials that have near epitaxially matched lattice constants, e.g., cadmium and mercury chalcogenides where the two cations have nearly identical radii.[24−26] In contrast, in most well-established core/shell particle systems such as Cd(Se,Te)/CdS and Cd(S,Se,Te)/ZnS, there exists a certain degree of lattice mismatch between core and shell. In some heterostructure combinations such as ZnSe/CdSe, cation diffusion enables the formation of an alloy or partial alloy core,[27] while in other combinations such as CdSe/CdS[28] and CdTe/CdS[29] the diffusion of the anions may lead to an anion gradient core. However, even in such cases some lattice mismatch remains in the system and will inevitably lead to strain.

There are two key consequences of strain for core/shell QDs constructed with mismatched materials—on one side the lattice will be under compression and on the other side it will be under tension. Due to the deformation pressure, conduction and valence bands in both core and shell will shift. As a result, the valence band offset (VBO) and the conduction band offset (CBO) between core and shell may both change accordingly, which significantly influences the optical properties of the QDs including absorption/emission band edges, recombination decay kinetics and transition oscillator strengths, etc. The strain may also induce or act upon defects at the interface, which could reduce the fluorescence efficiency.[27,30,31] All that said, lattice mismatch induced strain may not necessarily be a disadvantage, as it can be used as a tool to manipulate recombination rates in particular, but it should be properly accounted for in any model for the resulting electronic structure. Often in the literature, the strain effects are discussed qualitatively in terms of band deformation potential theory,[32] but there have been surprisingly few attempts to quantitatively include the strain effects into electronic structure models.[18] At present there are experimental approaches available such as scanning tunneling microscopy with spectroscopy that can allow the imaging of specific wave functions.[33−35] The effective mass approximation model (EMA) was adopted to simulate the wave functions, but the classic EMA is based on the bulk material conduction and valence potentials and does not take strain effects into consideration.[21,26] Therefore, it is critically important to provide insights into the impact of strains on electronic structure, the spatial distribution patterns of the charge carriers, and carrier recombination kinetics of strained core/shell QDs.

CdTe/CdS core/shell QDs are a good exemplar of a strained system since the mutual lattice mismatch is as large as 10%. Coating CdTe with CdS has been demonstrated to be an effective way to enhance the PL performance of CdTe QDs synthesized in an aqueous medium.[36,37] For example, by controlling the growth kinetics of the CdS shell via either a photo illumination-assisted process[36] or an ammonia-catalyzed process,[38] the room temperature PL QY of the core/shell QDs was boosted to 85%. More recently, it was demonstrated that aging magic-sized CdTe clusters (1.6 nm diameters) in aqueous solution containing Cd^{2+}−MPA (mercaptopropionic acid) complexes could produce CdTe/CdS core/shell particles with PL emission tunable from 480 to 820 nm.[37] In the former case, a type I core/shell structure was proposed, due to the dramatic PL enhancement accompanied by slight shift in the PL peak position. In the latter case, a type II structure was proposed as the PL emission peak position greatly shifted against the shell thickness,[32,37,39] which was also experimentally verified by the shell thickness-dependent PL lifetime. In the context of these contrary findings it is critically important to resolve the effect of strain on the electronic structure for a complete understanding of the diverse optical properties of CdTe/CdS QDs and of core/shell structured QDs in general.

Following our previous work on CdTe QDs,[36,38,40] we herein report our recent investigations on theoretical modeling of CdTe/CdS core/shell QDs with a strain-modified EMA. The lattice strain effects on the core/shell carrier potential alignments were investigated using measured strains and band deformation potential data. The rectified band offsets were then incorporated into the effective mass approximation (EMA) calculations for theoretical simulations of the electronic levels, carrier spatial distributions, and electron−hole wave function overlap. The simulation results were systematically compared with the optical properties experimentally derived through steady-state and transient spectroscopic studies. In particular, correlations of shell thickness with transition energies determined from absorption spectra, and electron−hole wave function overlap with oscillator strength derived from radiative recombination kinetics determined through time-resolved PL measurements were made.

EXPERIMENTAL SECTION

Chemicals. Cadmium perchlorate hexahydrate (Aldrich, 99.9%), thioglycolic acid (TGA) (Fluka, 97%+), L-glutathione reduced (GSH) (Sigma-Aldrich, ≥98.0%), and aluminum telluride (Al_2Te_3) (CERAC Inc., 99.5%) were used as received.

Synthesis of CdTe QDs. CdTe QDs stabilized by TGA were synthesized by introducing H_2Te (formed upon the reaction between Al_2Te_3 and diluted sulfuric acid) into an aqueous solution containing Cd^{2+} and TGA at pH 12.0 under nitrogen protection.[38,41,42] The feed ratio of Cd:Te:TGA was set to 1:0.58:1.30. The resulting reaction mixture was immediately refluxed under open-air conditions to generate CdTe QDs of desired sizes controlled by the refluxing time. Aliquots containing CdTe QDs with emission peak at 538 and 610 nm were extracted and are referred to as *as-prepared* $CdTe_{538}$ and $CdTe_{610}$, respectively, below.

Synthesis of CdTe/CdS Core/Shell QDs. By introducing isopropanol into the aliquots at room temperature, the as-prepared QDs were precipitated and collected by centrifugation. The particle precipitate was then redispersed in glutathione (GSH) solutions of 0.20, 1.00, 4.09, and 12.58 mmol/L, respectively. The initial pH of the GSH solutions was set to 9.8 by dropwise addition of 1 M NaOH solution prior to redispersion of the QDs. The final concentration of the QDs was of 3×10^{-3} mmol/L for all solutions. After deaerating using nitrogen for 30 min, the QD solutions were heated to reflux under open-air conditions, and the optical properties of the QDs were monitored throughout the reflux process using conventional absorption/fluorescence spectroscopy and time-resolved PL spectroscopy. The resulting QDs with initial emissions at 538 and 610 nm were denoted as $CdTe_{538}$ and $CdTe_{610}$ series, respectively, and this nomenclature is used throughout below.

Structural and Compositional Characterization. Transmission electron microscopy (TEM) images were recorded on a JEM-2100F

DOI: 10.1021/ja5127352
J. Am. Chem. Soc. 2015, 137, 2073−2084

microscope after calibration using a thin Au film. To improve the imaging contrast, QDs were transferred from water into toluene by utilizing OVDAC (octadecyl-*p*-vinylbenzyl-dimethylammonium chloride) as a phase transfer agent to avoid particle aggregation on the carbon supporting film of copper grids.[43] Powder X-ray diffraction (XRD) patterns of the QDs were recorded on a Regaku D/Max-2500 diffractometer. The composition of the QDs was determined by an inductively coupled plasma optical emission spectrometer (ICP-OES; Thermo Fisher iCAP6300) after the QDs were degraded by using a mixture of HCl/HNO_3 (aqua regia). The energy dispersive X-ray spectra were recorded on a Hitachi S4800 SEM operating at a beam energy of 10 kV.

Spectroscopic Characterization. Steady-state UV−Vis absorption and PL spectra were recorded at room temperature on a Cary 50 UV−Vis spectrophotometer and a Cary Eclipse fluorescence spectrophotometer, respectively. The excitation wavelength for all steady-state PL measurements was set to 400 nm. The PL QY of the QDs was estimated by using Rhodamine 6G as a fluorescence standard according to literature methods.[36] Time-resolved PL decay measurements were carried out on an Edinburgh Instruments FLS920P spectrometer equipped with a picosecond pulsed diode laser (EPL-405, pulse width: 49 ps) as a single wavelength excitation source (405 nm) for time-correlated single-photon counting (TCSPC) measurements.

Effective Mass Approximation Modeling. The EMA modeling of the electronic structure of the CdTe/CdS QDs was carried out according to previous reports in the literature.[21,44] The bandgap energies of bulk CdTe and CdS, i.e., 1.43[21] and 2.45 eV,[45] were adopted. The effective masses for electrons (m_e), heavy holes (m_{hh}), and light holes (m_{lh}) are given by $m_e(\mathrm{CdTe}) = 0.11m_0$, $m_e(\mathrm{CdS}) = 0.18m_0$, $m_{hh}(\mathrm{CdTe}) = 0.63m_0$, $m_{hh}(\mathrm{CdS}) = 1.43m_0$, $m_{lh}(\mathrm{CdTe}) = 0.12m_0$, $m_{lh}(\mathrm{CdS}) = 0.22m_0$, respectively, where m_0 is the free electron mass.[21,46,47] We note that the range of literature values for the CdS light hole mass has a wide spread. Here we adopted the value verified by both experiments and theoretical simulation.[47] A VBO of −1.17 eV as revised by Wei and co-workers[48,49] was used, which leads to a type II staggered structure from the outset (i.e., even without strain) for the CdTe/CdS heterostructure. The compressive and tensile strains were derived from HRTEM data for rectifying the energy levels of CdTe/CdS QDs with different shell thicknesses through the absolute volume deformation potentials reported by Wei and co-workers.[50] In addition, the average thickness of one monolayer of CdS shell was taken as 0.335 nm. By solving the radial Schrödinger equation, assuming Ben Daniel-Duke boundary conditions,[51] the EMA model allowed us to derive the band edge hole and electron states, in particular the single particle eigen energies and wave functions relating to the absorption and radiative recombination (PL) transitions for different core diameter and shell thickness combinations derived from experimental measurements. The square of the overlap integrals $|\int R_e^*(r)R_h(r)r^2\mathrm{d}r|^2$ of the electron and hole ground state radial wave functions R_e and R_h were also calculated for comparison with the oscillator strengths derived from the experimental radiative recombination rates at the band edge.

RESULTS AND DISCUSSION

Changes of Optical Properties of CdTe QDs with CdS Shell Growth. The absorption and PL spectra of $CdTe_{610}$ and $CdTe_{538}$ series QDs were carefully recorded during reflux in the presence of GSH. As shown in Figure 1a, the absorption onset of $CdTe_{610}$ QDs progressively shifted in 1.00 mmol/L GSH solution to lower energies against reflux time, and was accompanied by a red-shift of the PL emission. Along with these shifts, the PL intensity first increased and then slightly decreased after 9 h of reflux. The PL QY quickly increased during the initial 20 min reflux up to 54%. After that, it gradually decreased and became even lower than the initial QY at around 3 h of reflux. All these variations in optical properties were also observed during the refluxing of the aqueous solution

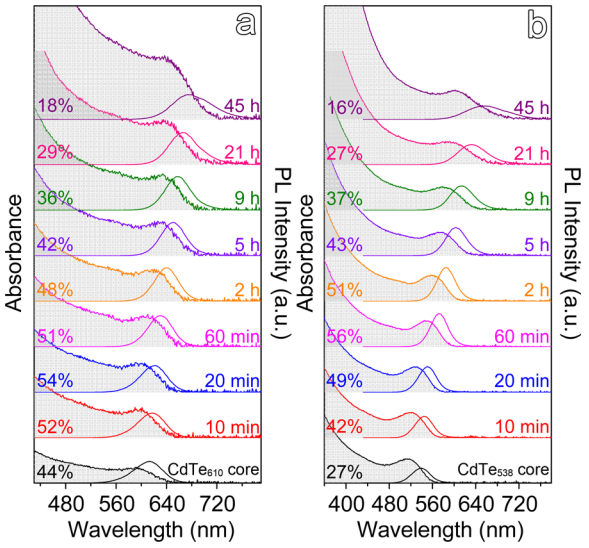

Figure 1. Temporal evolution of absorption and PL spectra of $CdTe_{610}$ (a) and $CdTe_{538}$ (b) series QDs recorded during reflux in 1.00 mmol/L GSH aqueous solutions, together with the PL QYs and reflux times as annotated.

of $CdTe_{538}$ QDs in the presence of GSH, but the PL shifted over a wavelength range as large as 100 nm after 45 h of reflux, as shown in Figure 1b. Moreover, the initial increment in PL QY was even more pronounced (from 27% to 56% after 60 min of reflux) than that for $CdTe_{610}$ QDs, and it took a longer time (21 h) for the PL QY to drop below the initial level.

A control experiment was carried out to probe the effect of possible substitution of TGA by GSH on the optical properties of CdTe QDs, since the first step binding constants (log K_1) of GSH and TGA for Cd^{2+} ions, i.e., 11.02[52] and 11.45,[42] are rather comparable. $CdTe_{610}$ QDs were incubated in GSH with a greatly increased concentration, i.e., 12.58 mmol/L. The incubation was carried out at room temperature rather than under reflux to avoid the thermal release of S^{2-}. GSH molecules could possibly act as additional surface capping molecules alongside the original TGA molecules due to the much higher GSH concentration. Nevertheless, after storing the reaction solution for one month at room temperature, such possible ligand redistribution did not lead to any obvious modification to the PL emission regarding the PL peak position and full width at half-maximum (fwhm), as shown in Figure S1 in the Supporting Information (SI). This suggests that the possible surface coordination of GSH does not substantially alter the optical properties of CdTe QDs.

It can therefore be deduced that overcoating of the CdTe QDs with a CdS shell has occurred and was responsible for the spectral changes observed during the reflux due to the thermally triggered release of sulfur from GSH in alkaline solution, because the pK_{sp} of CdS, i.e., 26.1,[53] is much higher than the binding constants of GSH and TGA for Cd^{2+} ions. At the deposition reaction front, GSH is less strongly attached, but allows the liberated S^{2-} in the solution to access the particle surface. The remarkable increase of absorbance at higher energies, as shown in Figure 1 and Figure S2, indicates the formation of a CdS shell upon the surface precipitation reaction between the released S^{2-} ions and the Cd^{2+} on the CdTe surface. This is supported by the increased S/Cd and S/Te ratios against reflux time shown in Figure S3 and Table S1. The formation of CdS on the surface of CdTe stabilized by TGA

DOI: 10.1021/ja5127352
J. Am. Chem. Soc. 2015, 137, 2073−2084

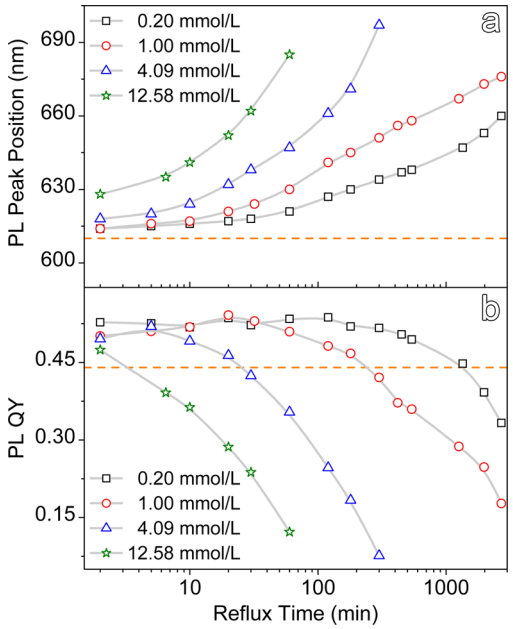

Figure 2. PL peak position (a) and PL QY (b) of $CdTe_{610}$ series QDs recorded during reflux in 0.20, 1.00, 4.09, and 12.58 mmol/L GSH aqueous solutions, respectively, with the corresponding initial values for the as-prepared $CdTe_{610}$ QDs shown as dashed lines.

was previously observed via a photo illumination-assisted[36] or an ammonia-catalyzed processes without any auxiliary addition of Cd precursor source,[38] but in both cases it typically took several or tens of days to degrade the TGA in order to release S^{2-} ions. Therefore, the enhancement of the PL QY during the initial reflux stage can be attributed to the elimination (passivation) of surface defects after the deposition of a wide bandgap semiconductor shell (CdS) on the narrow bandgap core (CdTe).[36]

To further investigate the impact of GSH concentration on the optical properties of CdTe QDs, three additional GSH solutions with concentrations of 0.20, 4.09, and 12.58 mmol/L, were prepared for comparative experiments on $CdTe_{610}$ QDs. In all these systems, the pH of the GSH solutions was kept the same to ensure identical thermal decomposition kinetics for sulfur release, and the concentration of the $CdTe_{610}$ QDs also remained the same as that for the previous experiment. The temporal evolutions of the PL peak position and PL QY of $CdTe_{610}$ QDs in these three systems were recorded during the reflux and compared with those based on the 1.00 mmol/L GSH solution. As shown in Figure 2a, the rate for red-shifting the PL peak position was strongly related to the GSH concentration. The initial offsets with reference to that for the as-prepared $CdTe_{610}$ (dashed line) are also different, because during the time period to heat the solutions from room temperature to the reflux point, different amounts of sulfide ions, depending on GSH concentration, were released prior to the commencement of reflux. The corresponding PL QYs in general undergo a similar enhancement process at the initial stage as shown in Figure 2b, but as the reaction continues, they all then gradually drop below the original value of 44% for the as-prepared $CdTe_{610}$ QDs with GSH concentration-dependent rates. The most important finding is that the PL shifting rate is strongly correlated with the eventual decline in the PL QY, indicating that the fast CdS shell growth kinetics has a significant adverse impact on the PL QY. For example, the

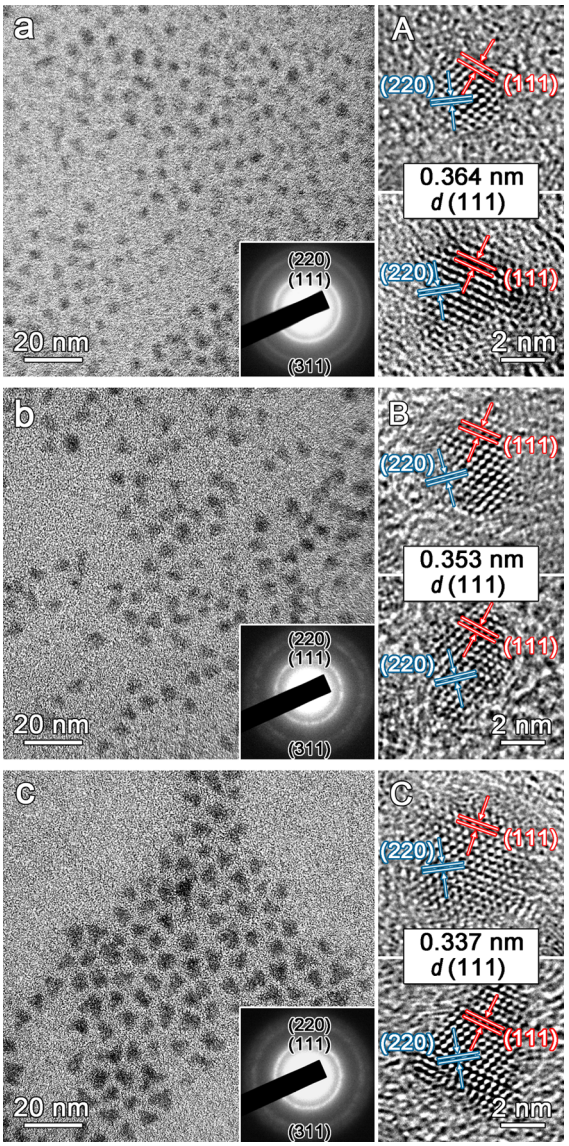

Figure 3. TEM and HRTEM images showing [$\bar{1}$10] projections, and SAED patterns of $CdTe_{610}$ series QDs obtained at reflux times of 5 h (b, B) and 45 h (c, C) in 1.00 mmol/L GSH aqueous solution for comparison with those recorded from the as-prepared $CdTe_{610}$ QDs (a, A).

lowest GSH concentration (0.20 mmol/L) allows the relatively long-term preservation of the PL QY above the initial value (44%) during a reflux interval up to ~22 h, while the highest concentration (12.58 mmol/L) starts to decrease the initially enhanced PL QY right after the commencement of reflux. Therefore, the subsequent decrease in PL QY observed upon prolonged reflux may be due to the increasing (compressive) strain on the core accompanying the shell thickening,[31] originating from the relatively large lattice mismatch (10%) between the zinc-blende forms of CdTe and CdS, which is discussed further in the following sections.

Structural Variations with CdS Shell Growth. Structural variations resulting from the progressive deposition of CdS shells were carefully studied by TEM and high resolution TEM (HRTEM). Representative TEM images of as-prepared $CdTe_{610}$ QDs and those obtained by being refluxed in 1.00 mmol/L GSH solution for different intervals are shown in Figure 3. In general, the particle size increases against reflux

DOI: 10.1021/ja5127352
J. Am. Chem. Soc. 2015, 137, 2073−2084

Table 1. Parameters for Multiexponential Fitting of Photoluminescence Decay Curves in Figure 4[a]

sample	QY [%]	λ_{em} [nm]	B_1 [%]	f_1 [%]	τ_i [ns]	B_2 [%]	f_2 [%]	τ_2 [ns]	τ_{avg} [ns]	τ_r [ns]	τ_{nr} [ns]	χ^2
$CdTe_{610}$ series QDs in the presence of GSH												
as-prepared	44.4	610	49.1	30.2	11.9	50.9	69.8	26.5	22.1	49.8	39.5	1.207
10 min	51.8	621	36.7	22.7	14.4	63.3	77.3	28.4	25.3	48.8	52.5	1.065
2 h	48.2	649	40.5	26.1	19.2	59.5	73.9	37.0	32.3	67.1	62.3	1.088
21 h	28.7	671	37.5	19.3	21.3	62.5	80.7	53.2	47.1	164.0	66.1	1.095
45 h	17.7	685	34.8	14.5	20.2	65.2	85.5	63.6	57.3	323.4	69.3	1.147
$CdTe_{610}$ series QDs in the absence of GSH												
as-prepared	44.4	610	49.1	30.2	11.9	50.9	69.8	26.5	22.1	49.8	39.5	1.207
10 min	43.2	619	47.6	31.4	14.3	52.4	68.6	28.4	24.0	55.5	42.3	1.111
2 h	45.3	625	54.8	40.2	17.9	45.2	59.8	32.4	26.6	58.7	48.7	1.157
21 h	42.2	639	43.9	28.5	16.1	56.1	71.5	31.5	27.1	64.3	46.8	1.083
45 h	37.1	649	41.4	25.3	15.2	58.6	74.7	31.7	27.5	74.1	43.7	1.093

[a]Normalized amplitude B_i, time constant τ_i, and their normalized products f_i, goodness-of-fit parameter χ^2, together with the experimentally determined QY and emission peak position (the expressions for f_i, τ_r, and τ_{nr} are given in the SI).

time. For example, the average diameters of the as-prepared QDs and those extracted by reflux times of 5 and 45 h were determined to be 3.7 ± 0.5 nm, 4.2 ± 0.6 nm, and 5.5 ± 1.0 nm, respectively, by averaging over at least 1000 particles for each measurement. The corresponding size histograms are provided in Figure S4 in SI. Given the thickness of 0.335 nm for single monolayer CdS, the CdS shell on the CdTe/CdS particles obtained at reflux times of 5 and 45 h roughly contain ~0.7 and ~2.7 monolayers, respectively, by assuming that the initial CdTe core did not change during the CdS shell coating. In a very similar way, the average size of as-prepared $CdTe_{538}$ QDs increased from 2.8 ± 0.4 nm, to 3.6 ± 0.5 nm (2 h) and 4.0 ± 0.6 nm (21 h), respectively, after being refluxed in 1.00 mmol/L GSH solution. These size increments correspond to approximately ~1.2 and ~1.8 CdS monolayers. The detailed TEM, HRTEM, and particle size histograms of $CdTe_{538}$ series QDs are provided in Figure S5.

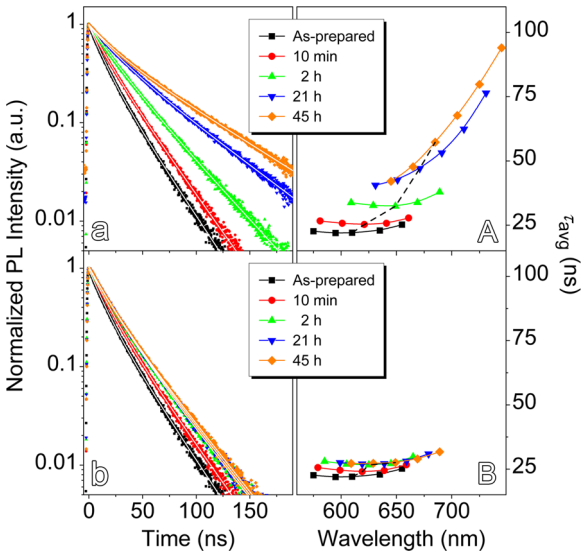

Figure 4. Normalized time-resolved PL decay curves (a, b) and corresponding wavelength-dependent time-resolved PL average lifetimes (A, B) as a function of reflux time for $CdTe_{610}$ series QDs in 1.00 mmol/L GSH aqueous solution (a, A), and in aqueous solutions with no GSH (b, B), with the corresponding lifetimes at the PL peak positions shown as dashed lines (A, B).

The interplanar spacing across the whole of the particle lattice was seen to be progressively reduced during the CdS shell growth, as supported by powder X-ray diffraction results shown in Figure S6. According to the HRTEM results given in Figures 3A–C, the interplanar distance of (111) crystal lattice planes was 0.364 nm for the as-prepared $CdTe_{610}$, slightly smaller than that (L_0 = 0.370 nm) for bulk zinc-blende CdTe. The (111) interplanar spacing contracted to 0.353 nm (5 h) and further to 0.337 nm (45 h) upon reflux. The well-resolved SAED patterns (insets in Figure 3a–c) further confirm the preservation of the cubic zinc-blende phase throughout the shell coating process. Considering the fact that bulk cubic zinc-blende CdS possesses a much smaller interplanar distance for (111) planes, i.e., L_0 = 0.335 nm, the lattice compression can be attributed to the influence of the CdS shell coating, which inevitably leads to strain in the CdTe cores. With respect to $CdTe_{538}$ series QDs, the initial lattice spacing for the (111) planes was 0.360 nm and dropped to 0.347 nm (2 h) and further to 0.336 nm (21 h) during the reflux. In addition, similar to previous observations,[54] both tetrahedral and partially truncated tetrahedral morphologies represent the majority of the as-prepared CdTe QDs as shown in Figure 3a and 3A. This tetrahedral-based morphology was maintained through the CdS shell growth in GSH media as shown in Figure 3b,c and 3B,C, suggesting that the shell growth took place rather homogeneously on the core surface. It is deserved to mention that in every case lattice planes in the HRTEM images stretch across the entire nanocrystal with no evidence of a discontinuity, thus maintaining the lattice arrangement throughout the CdS shell. This indicates coherent epitaxial shell growth in spite of the shell induced strain.

The PL fwhm of $CdTe_{610}$ QDs was also recorded during the reflux process. As shown in Figure S7, both the PL fwhm and normalized PL fwhm (PL fwhm/peak wavelength) were gradually narrowed against reflux time up to 9 h, suggesting that the initial stage of the reflux slightly narrowed the particles size distribution. Considering the smaller Cd–Te bond dissociation energy of 100.0 kJ/mol with respect to that of Cd–S (208.5 kJ/mol),[55] Ostwald ripening is more likely to happen for CdTe than for CdS. In consequence, the redissolution of smaller CdTe QDs or QDs bearing high-density surface disorders/defects, very likely nonfluorescent CdTe particles, furnishes the required Cd^{2+} ions for growing thicker CdS shell in the presence of S^{2-} ions. In addition, it was also found out that Cd-TGA complex as the precursor of CdTe

DOI: 10.1021/ja5127352
J. Am. Chem. Soc. 2015, 137, 2073–2084

QDs provided an additional source of Cd^{2+} ions as the excess Cd-TGA complex can be precipitated by isopropanol. Further ICP-OES measurements revealed that unreacted Cd up to 20% with reference to that of $CdTe_{610}$ QDs was precipitated by isopropanol according to the experimental procedures described in the Experimental Section.

Charge Carrier Recombination Kinetics Studies. The charge carrier recombination kinetics as a function of CdS shell growth was studied by time-resolved PL measurements. Figure 4a shows representative PL decay curves measured at the PL emission peak wavelengths (λ_{max}) of $CdTe_{610}$ QDs as a function of reflux time in GSH solution. The PL relaxation is generally characterized by a multiexponential decay process. The best decay fits obtained by a biexponential function are summarized in Table 1. A general trend to be noted is that the average decay lifetime (τ_{avg}, see Supporting Information for definition) increases with the reflux time, from 22.1 ns (as-prepared) to 57.3 ns after 45 h of reflux. Given the PL QY of $CdTe_{610}$ QDs, the average radiative recombination lifetime (τ_r) significantly increases from 49.8 ns (as-prepared) to 323.4 ns (45 h), suggesting a reduced electron−hole wave function overlap against shell thickening (the systematic error was approximately ± 0.5 ns for all lifetime measurements). The nonradiative recombination lifetimes (τ_{nr}) also increased from 39.5 ns (as-prepared) to 69.3 ns (45 h), less markedly than the radiative lifetime. A similar trend was also found for $CdTe_{538}$ QDs as shown in Figure S8.

There was no sign of any additional decay components throughout the GSH treatment, suggesting that there were no new recombination centers formed as a consequence of CdS coating. In addition, the lifetime of the existing nonradiative recombination channel increased as the reflux proceeded, and the recombination channels associated with the slow decay component progressively dominated the overall PL emission. For example, the component amplitudes (B_2) and their corresponding lifetime-amplitude products (f_2) increased from 50.9% (as-prepared) to 65.2% (45 h), and from 69.8% (as-prepared) to 85.5% (45 h), respectively (Table 1). The enhancement of the slow component should be correlated to variation in the electronic structure and carrier spatial distribution during shell growth and this is discussed in relation to theoretical simulations in the following section.

In order to compare the effect of any structural consolidation (e.g., annealing of the lattice or changes in surface states) as a consequence of the heating process (i.e., not arising from the GSH thermal decomposition), the PL decay curves of $CdTe_{610}$ QDs obtained upon reflux in the absence of GSH are presented in Figure 4b. Similar fitting revealed that τ_{avg} and τ_r increased slightly from 22.1 ns (as-prepared) to 27.5 ns (45 h), and from 49.8 ns (as-prepared) to 74.1 ns (45 h), respectively, and the nonradiative lifetimes were mainly located in a narrower range of 39.5−48.7 ns (Table 1). In addition, the slow component contributing to the emission process remained relatively constant, i.e., from 69.8% to 74.7% over the same time scale. This further suggests that the formation of the CdTe/CdS core/shell structure substantially alters the transient PL behaviors.

In addition to PL decay lifetime measurements carried out at the PL peak position, the spectrally resolved PL lifetimes were also measured over a broader range of wavelengths on both sides of the PL peak maximum. The average decay lifetime exhibited an enhanced wavelength-dependent behavior with reflux time for $CdTe_{610}$-in-GSH, as shown in Figure 4A. In contrast, as shown in Figure 4B, both as-prepared CdTe QDs and those obtained by refluxing in the absence of GSH show similar average PL decay lifetimes across the wavelength range covering the PL peak position, again suggesting that the formation of the CdTe/CdS core/shell structure greatly increased the PL lifetimes (Table 1 and Tables S2−S4). Taking the $CdTe_{610}$ QDs obtained after 45 h of reflux as an example, the lifetime of the PL centered at 685 nm increased from 42.1 ns (645 nm) to 94.0 ns (745 nm). The extended PL lifetimes suggest that the CdS coating may not be uniformly shared across the QD ensemble at long reflux times. Nevertheless, even for the population of CdTe QDs with thinner CdS shells, the lifetime of emission observed at 645 nm is substantially higher than the PL lifetimes of $CdTe_{610}$ QDs extracted at 2 h of reflux. This demonstrates that the growth of thicker CdS shell can substantially prolong the PL lifetime of the QDs by forming a Type II band alignment structure.[37] Moreover, the relatively weak PL wavelength dependent lifetime for CdTe/CdS core/shell QDs with thinner CdS shell (achieved before 2 h of reflux) suggests that at that stage the CdTe cores were more evenly coated. This gave rise to the enhanced PL observed here and is consistent with our previous observations on coating CdTe with CdS shells with much slower S^{2-} supply rates via either an illumination-assisted process[36] or an ammonia-incubation process.[38] Since the fast fluorescence enhancing process is accompanied by slow PL red-shift during the early stage of reflux, it can be deduced that CdTe QDs coated with thinner CdS shell present a more Type I-like band alignment structure. Therefore, it is interesting to learn how the electronic structure of the CdTe/CdS core/shell QDs evolves against the thickness of the CdS shell.

Electronic Structure Modeling of CdTe/CdS Core/Shell QDs. The physical effects of the CdS shell on CdTe cores were theoretically modeled using the EMA approach. In detail, comparisons with data derived from the experimentally measured optical spectra were made with respect to band edge absorption and emission wavelengths, band edge oscillator strengths, and PL lifetimes. On the basis of the bandgap energies and VBOs of bulk CdTe and CdS, in combination with the lattice evolution observed during shell growth, energy level structures were specifically rectified on which to base the calculation of the overall eigen energies for electrons and (light and heavy) holes in their confined states, and the wave functions of the respective carriers.

Strain Modified Band Alignment. There have been a number of previous studies on core/shell QD systems where the addition of a shell layer with smaller lattice constant produces a sufficient shift in the respective bandgaps to bring about a change from type I to type II heterostructure behavior. These include CdSe/ZnSe,[19,20] and CdTe coated with a number of other II−VI shells.[18,56] Some earlier studies assumed a type I structure for CdTe/CdS core/shell QDs since the CBO would be around 0.02−0.07 eV if the VBO is −0.99 eV.[32,48] However, a more recent revision of the VBO down to −1.17 eV[49] will change the sign of the CBO to negative and make the CdTe/CdS core/shell particle type II structure even without including the effect of strain.

As already mentioned, the lattice mismatch between CdTe and CdS will place the shell under tension as it tries to accommodate the larger lattice spacing of the core, while the latter will experience a compressive strain due to the shell. In order to fully account for these strain effects, the respective bandgaps of core and shell as well as CBOs and VBOs were

DOI: 10.1021/ja5127352
J. Am. Chem. Soc. 2015, 137, 2073−2084

Table 2. Experimentally Determined Lattice Parameters (L) Together with the Pressure Increments (ΔP) Calculated by Using the above Data for CdTe/CdS Core/Shell QDs Obtained by Different Reflux Times[a]

		$\Delta L/L_0$		ΔP (kbar)	
sample	L (nm)	CdTe	CdS	CdTe	CdS
$CdTe_{610}$ series					
5 h	0.353	−0.046	0.054	61	−67
45 h	0.337	−0.089	0.006	119	−7
$CdTe_{538}$ series					
2 h	0.347	−0.062	0.036	83	−44
21 h	0.336	−0.092	0.003	123	−4

[a]A negative ΔP value represents tensile strain and a positive value indicates compressive strain.

modified using band deformation potential theory with experimentally determined strain-induced pressures.

Experimentally the compressive and tensile strains within CdTe/CdS core/shell QDs were determined according to the variation of interplanar spacing of (111) planes based on HRTEM results shown in Figure 3A−C. Since the measured lattice spacing fell between those for CdTe (L_0 = 0.370 nm) and CdS (L_0 = 0.335 nm), the lattice mismatch introduces compressive strain to the CdTe core and tensile strain to CdS shell as the two regions adopt an identical intermediate spacing to retain the epitaxial registration. The strain-induced pressure increments (ΔP) in the two domains can be calculated by using the bulk modulus (B: 445 kbar for CdTe and 620 kbar for CdS)[50] and the fractional change in lattice constants ($\Delta L/L_0$) relative to the undistorted case. Assuming the strain is isotropic, ΔP in the core can be described by

$$\Delta P = -3B\Delta L/L_0 \quad (1)$$

We further assume that for single and few monolayer coatings the relative volume change in the shell is mainly due to tangential strain with little or no radial contribution. Thus, ΔP in the shell can be expressed as

$$\Delta P = -2B\Delta L/L_0 \quad (2)$$

By using eqs 1 and 2, compressive (CdTe) and tensile (CdS) pressures were calculated and are given in Table 2 for the $CdTe_{610}$ and $CdTe_{538}$ series QDs. The pressures, ranging from 4 to 123 kbar (0.4 to 12.3 GPa), fall in the typical range of strain-induced pressures in II−VI heterostructures.[57] We stress that this is a simplified approach; in other studies, where the core and shell dimensions were larger and the QDs were more spherical in nature, continuum elastic strain analysis in spherical geometries could be considered.[18] However, the QDs in the current study are smaller (typically 2.8−5.5 nm, shells only up to ~2.7 ML in thickness), so such detailed strain analysis is not justified. In addition, no evidence of any radial strain gradient was observed in such small QDs; therefore, simple isotropic strain was assumed herein. In larger core/shells reported by Cai et al.[57] (3.4 nm CdTe core, >5 ML CdSe shell) and Smith et al.[18] (3.8 nm CdTe core, 6 ML ZnSe shell), a multiple concentric sphere model was adopted to incorporate radial strain gradients into their strain analyses. They point out that the thicker shells will experience not only tangential tensile strain but also radial compression. However, the latter will be absent with single and few monolayer shells, so the radial shell compression was neglected in the current approach.

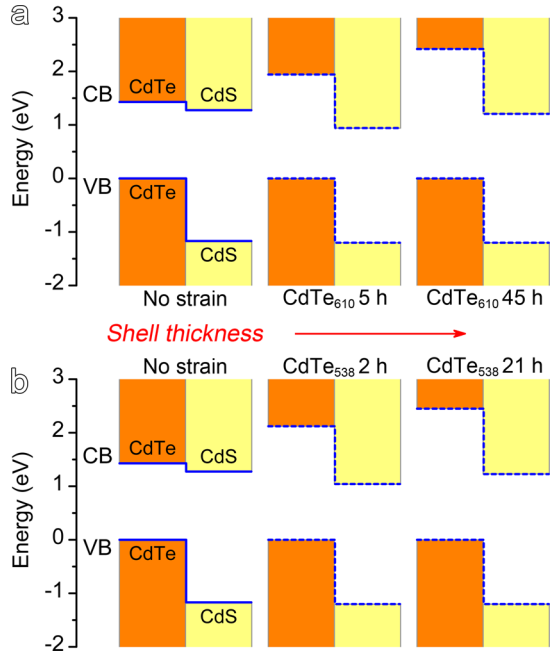

Figure 5. Calculated band alignments for CdTe/CdS core/shell QDs based on the corresponding bulk bandgap values and strain-induced band shifts for $CdTe_{610}$ QDs (a) and $CdTe_{538}$ (b) series QDs based on strain measurements at different reflux times (middle, right) and for comparison with those in the absence of strain (left).

In principle, once the strain-induced pressure (ΔP) is known, the strain effect on the bulk conduction and valence band levels of both core and shell, and their band offsets, can be calculated from valence and conduction band deformation potentials. The relationship between the volume deformation potential (a_v) and pressure deformation potential (a_p) is given by

$$a_p = -a_v/B = \Delta E_{VB,CB}/\Delta P \quad (3)$$

where $\Delta E_{VB,CB}$ is the strain-induced energy shift in the valence or conduction band. For the core, with eq 1 and eq 3 it gives

$$\Delta E_{VB,CB} = 3a_v\Delta L/L_0 \quad (4)$$

and for the shell, with eq 2 and eq 3 it gives

$$\Delta E_{VB,CB} = 2a_v\Delta L/L_0 \quad (5)$$

In eqs 4 and 5, a_v for the conduction band and valence band of CdTe is −2.81 and 0.89 eV, respectively, and the corresponding values for CdS are −2.54 and 0.40 eV, respectively.[50] The variation of the valence band offset, ΔE_{VBO} was then calculated according to Akinci's expression:[58]

$$\Delta E_{VBO} = (\Delta E_{VB}/\varepsilon_\infty)_{CdTe} - (\Delta E_{VB}/\varepsilon_\infty)_{CdS} \quad (6)$$

where ε_∞ is the optical frequency permittivity of the material, i.e., 7.2 (CdTe) and 5.2 (CdS).[58]

The strain-induced modifications to the bulk band structures according to the strain pressures of $CdTe_{610}$ and $CdTe_{538}$ series QDs given in Table 2 are listed in Table S5. The resulting band structures are schematically drawn in Figure 5. Core compression forces the CdTe conduction and valence levels apart, while tension in the shell draws the corresponding levels together. However, the tension in the shell falls rapidly as the shell thickens, while the compression in the core continues to increase. Thus, the initial contraction of the shell bandgap is

DOI: 10.1021/ja5127352
J. Am. Chem. Soc. 2015, 137, 2073−2084

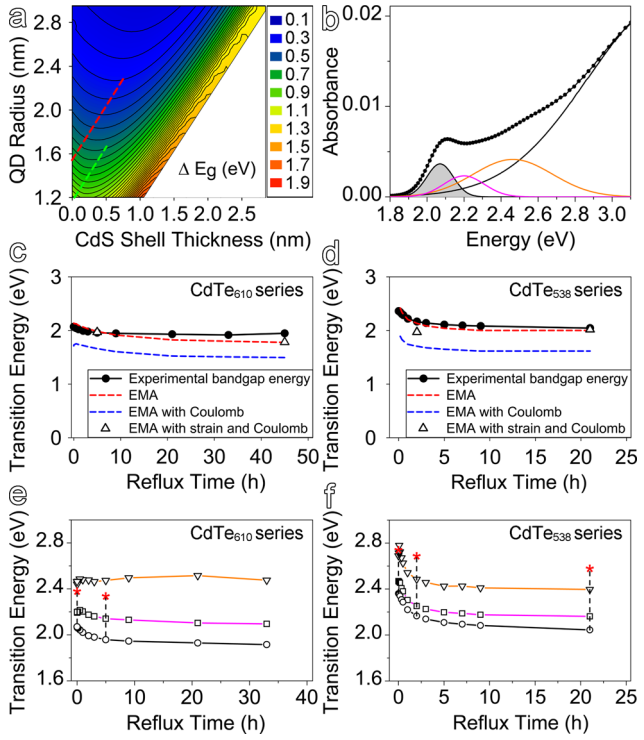

Figure 6. (a) A contour plot of the confinement part of the bandgap energies (the difference between the QD and bulk material bandgaps) against QD radius and CdS shell thickness overlaid with the paths for $CdTe_{610}$ (red dashed line) and $CdTe_{538}$ (green dashed line) series QDs calculated by using simple EMA method. (b) A representative absorption spectrum of CdTe/CdS QDs fitted to a sum of four Gaussians. (c, d) The evolution of bandgap energies ($1S_e-1S_{hh}$) against reflux time compared with the calculated data obtained with simple EMA (red dashed line), EMA taking Coulomb factor (blue dashed line) and EMA taking both Coulomb and strain factors into consideration (hollow triangles), for $CdTe_{610}$ (c) and $CdTe_{538}$ (d) series QDs. (e, f) The fitted Gaussian absorption peak energies against reflux time for $CdTe_{610}$ (e) and $CdTe_{538}$ (f) series QDs overlaid with vertical dashed vertical lines indicating the calculated $1S_e-1S_{lh}$ transition (stars) for selected samples.

reversed toward the nonstrained value as the tension falls with shell thickening, while the core bandgap rises as the compression continues to mount. The VBO stays nearly constant because the valence band contributions of core and shell partially compensate each other according to eq 6, while the CBO is significantly larger than that for the nonstrained case and continues to increase with the shell growth as shown in Figure 5 and Table S5.

Strain Effects on Optical Transition of CdTe/CdS QDs. In principle, the EMA method allows the calculations of bandgap energy of CdTe/CdS core/shell QDs with different core size and shell thickness. Figure 6a presents a contour map of the confinement contribution to the shift in the bandgap energies relative to the bulk material plotted against the overall size of the core/shell QDs and CdS shell thickness. Since the EMA model assumes a simple spherical core−shell geometry whereas in reality the particles are tetrahedral in habit, the TEM sizes were slightly rescaled. Allan and Delerue observed in tight binding model studies of simple QDs that differently shaped structures gave matching transition energies when the QD volumes were equal.[59] Tetrahedra with sides of equal length (l) have volumes equivalent to those of a sphere with diameter approximately $0.61 \times l$. If instead of measuring the edge length of the tetrahedra, the perpendicular distance between a side and the opposite vertex is measured, the diameter to measured size scaling factor is $0.70 \times l$. However, it can be seen in Figure 3 that a significant number of QDs are missing one or more vertices, which makes factoring in the geometry somewhat difficult. Instead, we measured the sizes from midedge to opposite corner (truncated or otherwise). The average geometry correction factor was then determined by comparing the measured absorption band edge with the size-bandgap energy curve for quasi-spherical CdTe QDs given by Kamal to calculate the equivalent spherical diameter.[60] This gives a slightly higher correction factor of $0.83 \times l$, which effectively takes into account the fact that many but not all of the vertices of our QDs were missing. Using this approach, the bandgap energies were calculated with EMA and shown as dashed lines for particles with (scaled) radius and shell thickness in Figure 6a. These theoretical data were further compared with the experimental results below.

In order to qualitatively understand the shell thickness-dependent optical absorption, the absorption spectra ($A(E)$) were fitted to the sum of four Gaussian peak functions (Figure 6b) in a manner similar to that recently used by Smith et al.[26] with the following equation:

$$A(E) = \sum_{i=1}^{4} A_i e^{-((E-E_{\mathrm{peak}_i})/2w_i)^2} \tag{7}$$

where E_{peak} and w are the peak position energy and width of each component. The lowest energy peak was taken as the bandgap energy and its variation with reflux time, together with those interpolated from the EMA bandgap contour map without strain or Coulomb factors in Figure 6a are shown in Figure 6c ($CdTe_{610}$) and Figure 6d ($CdTe_{538}$). The agreement between experiment and simple EMA theory appears to be fortuitously good at this stage. However, there are two further factors that must also be considered, i.e., the strain-induced shifts in the electron and hole energy levels via their deformation potentials and the reduction in exciton energies due to the Coulomb attraction between the confined carriers. The accurate determination of Coulomb effects on the total energy for particles with realistic shapes (mostly tetrahedra, frequently with truncated vertices) is a rather complex problem. Even accounting for the shape, the addition of shell material, particularly for average surface coverage below one monolayer of CdS, may not be uniform due to the differences in the binding energies at sites on vertices and edges compared with that at the centers of tetrahedral faces for example.

The rigorous calculation of the Coulomb contribution to the total energy (E_c) in a realistically shaped heterostructure remains difficult. It can be formally included in first order perturbation theory as a term given by[44]

$$E_c = \frac{-e^2}{4\pi\varepsilon_0} \iint \mathrm{d}r_e \mathrm{d}r_h r_e^2 r_h^2 \frac{|R_e(r_e)|^2 |R_h(r_h)|^2}{\max(r_e, r_h)} \times \frac{1}{\bar{\varepsilon}_r(r_e, r_h)} \tag{8}$$

where r_e and r_h are the radial electron and hole positions, $R_e(r_e)$ and $R_h(r_h)$ are radial 1S wave functions of the respective carriers, and $\bar{\varepsilon}_r(r_e, r_h)$ is the mean (weighted) dielectric constant of the material between the electron and hole. Brus originally gave a simpler expression for the Coulomb energy between the lowest electron and hole states in his particle system in a box model as[61]

DOI: 10.1021/ja5127352
J. Am. Chem. Soc. 2015, 137, 2073−2084

$$E_c = -\frac{1.8e^2}{\varepsilon_r r} \quad (9)$$

but also calculated the same energy term more accurately using a variational method for simple spherical CdS QDs ranging in radius from r = 2 to 5 nm with a single dielectric constant ε_r. The results of Brus' variational calculation for the Coulomb energy at a range of QD radii can be equated with the simple expression for E_c in eq 9, introducing a simple additional proportionality factor that depends linearly upon r to take account of the slightly different radial dependence of the two calculation methods. This then allows the modification of eq 9 to extrapolate to the QD radii used in our study, details are provided in the SI. For the Coulomb energy calculation we make the simplifying approximation that our QDs are simply pure CdTe and r is the radius of the entire core/shell QD.

However, as seen in Figures 6c and 6d, including the Coulomb term with the EMA model as outlined above leads to rather poorer agreement with experimental data for the bandgap transition, with an underestimate of several hundred meV in each case, with a slightly worse discrepancy for the smaller $CdTe_{538}$ series QDs. Nevertheless, it was found that the Coulomb term is largely offset if the strain effect on the conduction and valence bands is taken into consideration, as shown by the triangles in Figures 6c and 6d, which leads to excellent agreement between the simulation results and the experimental data.

Subject to the earlier caveats given regarding the uncertainty in the light hole masses for CdS,[47] the energy gap for transitions involving the 1S electron ($1S_e$) and 1S light hole ($1S_{lh}$) in the core/shell heterostructure were calculated with the strain-modified EMA model in order to compare with the fitted higher energy absorption peaks. It was assumed that the same band deformation potentials for the conduction and valence bands were applicable as for the treatment of the heavy hole case. By further assuming the Coulomb energies are of a broadly similar magnitude for transitions involving the heavy hole and light hole, the energy difference between the $1S_e-1S_{hh}$ and the $1S_e-1S_{lh}$ transitions were estimated at a number of shell thicknesses. These difference values were further added to the experimental ($1S_e-1S_{hh}$) bandgap energies to show the predicted likely location of the $1S_e-1S_{lh}$ transitions. Since the resulting values as indicated by the red stars at the upper end of the dashed guide lines in Figures 6e and 6f are much closer to the third highest energy fitted peaks (orange curves), the second highest energy fitted peaks (pink curves) more likely arise from higher order electron–heavy hole transitions than from the $1S_e-1S_{lh}$ absorption process.

Strain Effects on Charge Carrier Recombination Kinetics. The wave functions of $1S_e$, $1S_{hh}$, and $1S_{lh}$ levels for the $CdTe_{610}$ and $CdTe_{538}$ series QDs before and after being coated with CdS shells at different reflux intervals were calculated. In all these cases, the energy eigen values and resulting wave functions were determined taking account of the conduction and valence band shifts due to strain. As shown in Figure 7a and 7b, introducing thin CdS shells, e.g., ~0.7 ML for $CdTe_{610}$ (5 h) and ~1.2 ML for $CdTe_{538}$ (2 h), slightly reduces the overlap of electron and hole wave functions that are initially confined in the core, and leads to slight extension of electron and light holes into the shell. But the separation of electron and heavy hole wave functions remains not very substantial at this stage. The electron–heavy hole overlap at this thin shell stage is not very much lower than that for type I alignment, which may

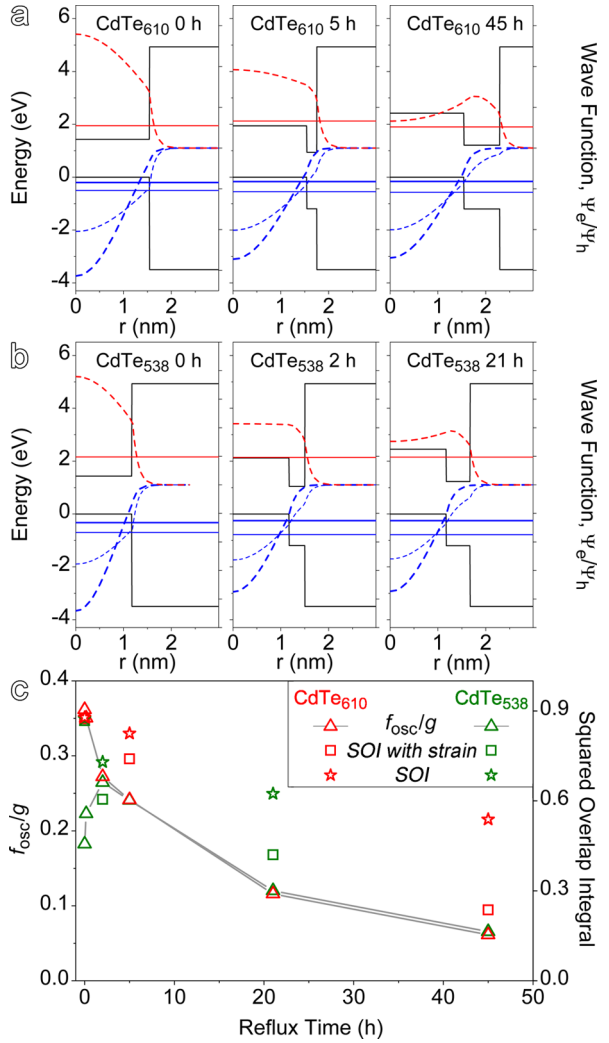

Figure 7. (a, b) Radial conduction and valence potentials overlaid with calculated electron (upper solid red lines), heavy (bold solid blue lines) and light (solid blue lines) hole eigen energies, and electron wave function (red dashed line), heavy (bold blue dashed line) and light (blue dashed line) hole wave functions for $CdTe_{610}$ (a) and $CdTe_{538}$ QDs (b) obtained by reflux times as indicated. (c) Experimentally determined f_{osc}/g values and the squared overlap integral (SOI) values calculated with strained-modified EMA (*SOI with strain*) and simple EMA (*SOI*) against reflux time.

explain earlier claims of type I structures for CdTe/CdS core/shell QDs obtained by the photo illumination-assisted[36] or ammonia-catalyzed processes.[38] It is worth of mentioning that the latter processes usually took much longer times (24 days for the illumination-assisted process and 8 days for the ammonia-catalyzed process) to reach the corresponding PL QY maxima (>80%). According to the electron/hole wave functions simulated in the absence of strain as shown in Figure S9, the extension of the electron wave function into the shell is greatly reduced. Since the heave hole wave function remains strongly located in the core, the CdTe/CdS more likely behaves like a pseudo-type I QD in the absence of strain. However, in the presence of strain, the electron wave function further extends into the CdS shell with higher thickness, e.g., ~2.7 ML for $CdTe_{610}$ and ~1.8 ML for $CdTe_{538}$ as shown in the right-hand frames of Figure 7a,b, while the heavy hole wave function remains localized in the CdTe core. In consequence, the CdTe/

DOI: 10.1021/ja5127352
J. Am. Chem. Soc. 2015, 137, 2073–2084

CdS behave more clearly like type II QDs in the presence of strain, which should lead to decreased probability of radiative recombination and prolonged exciton lifetimes.

On the basis of the strain effect upon the wave function localization of electron and hole, the wave function overlap was further calculated and compared with the experimental results to verify our hypothesis. In principle, the squared overlap integral $|\int R_e^*(r)R_h(r)r^2dr|^2$ of the electron and hole ground states is proportional to the transition oscillator strength. The heavy hole state with radial wave function $R_{hh}(r)$ was considered here. The overlap function can be compared with the calculated oscillator strength (f_{osc}) derived from the PL radiative recombination rate (τ_r^{-1}) based on Fermi's Golden Rule. The f_{osc} is given in cgs units by:[60,62]

$$f_{osc} = \tau_r^{-1} \times \frac{m_0 c^3}{2e^2\omega^2 n_s} \times \frac{1}{f_{lf}^2} \times g \quad (10)$$

where f_{lf} is a local field factor for QDs surrounded by solvent with refractive index n_s; e is the electronic charge; ω is the frequency; c is the velocity of light in vacuum; m_0 is the electron mass; and g is the degeneracy for the transition associated with the total number of accessible exciton states. For CdTe in isolation it would be assumed that $g = 8$, though Kamal et al. found better agreement with data derived from average relaxation rates (the net of radiative and nonradiative rates) with $g = 16$, suggesting that the involvement of additional dark exciton transitions may be responsible this higher value.[60] In the present case, the degeneracy value is not so clear because the presence of strain may cause degenerate levels to split and, if sufficiently so, the degeneracy of the remaining levels at the band edge may be expected to fall. For comparisons with the overlap we therefore chose to use f_{osc}/g which essentially represents the transition strength per degenerate level, but (apart from a nominally constant scaling factor) this should still have the same shell thickness dependence as the overlap function.

The local field factor (f_{lf}) can be calculated from the refractive index of the QDs (n_{QD}) based on the weighted percentage of CdS and CdTe derived from EDX analysis, and that of the solvent (n_s) by

$$f_{lf}^2 = \left(\frac{3n_s^2}{n_{QD}^2 + 2n_s^2}\right)^2 \quad (11)$$

The calculated f_{lf}^2 for both $CdTe_{538}$ and $CdTe_{610}$ QDs obtained at different reflux intervals are shown in Figure S10.

The radiative recombination rate τ_r^{-1} can be determined experimentally from the quantum yield (QY) and the measured average recombination rate τ_{avg}^{-1} as follows:

$$\tau_r^{-1} = QY \times \tau_{avg}^{-1} \quad (12)$$

The oscillator strength divided by the net level degeneracy (g), i.e., f_{osc}/g, is plotted against reflux time as shown in Figure 7c. Before CdS shell coating, the f_{osc}/g values for $CdTe_{610}$ and $CdTe_{538}$ cores are different by almost a factor of 2, which could probably be explained by a difference in level degeneracy, e.g., $g = 16$ for $CdTe_{538}$ and $g = 8$ for $CdTe_{610}$ at this stage.[60] It is interesting to further find out that (if this is the case) as the CdS shell thickness increases, the degeneracy for smaller CdTe QDs is partly lifted by 2 h of reflux. Thereafter, the oscillator strength becomes independent of the initial core size (for both $CdTe_{610}$ and $CdTe_{538}$ series QDs the trends after 2 h are virtually identical), quite probably due to the enhanced strain effect, because the shell growth is much faster during the early stage of reflux if taking the decomposition kinetics of GSH into consideration.

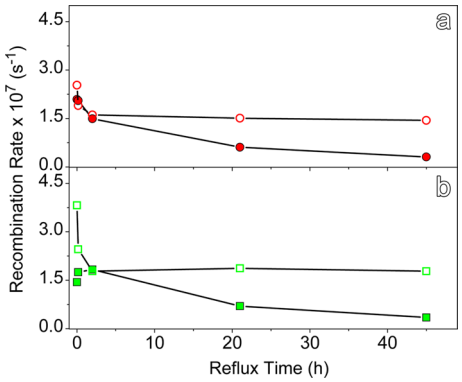

Figure 8. Radiative (solid) and nonradiative (hollow) recombination rates for $CdTe_{610}$ (a) and $CdTe_{538}$ (b) series QDs obtained at different reflux times.

By further comparing experimental oscillator strength data with the theoretical results (squared electron–hole wave function overlap integral), taking strain effects into consideration, it can be seen that for both $CdTe_{610}$ and $CdTe_{538}$ series QDs the trends with reflux at times longer than 2 h give a very good match between the two. In contrast, poor agreement between the experimental data and the theoretical results derived from EMA calculations without strain (as also given in Figure 7c) seems to offer further support that strain-induced variation of the CBO is necessary to explain the impact of the localization of the electron/hole wave functions especially when the shell is considerably thick.

It is therefore interesting to further correlate the radiative and nonradiative recombination rates with the PL QY to understand the fluorescence behavior of the strained QDs with the CdS shell thickness. The nonradiative relaxation rate τ_{nr}^{-1} can be expressed as

$$\tau_{nr}^{-1} = \tau_{avg}^{-1} - \tau_r^{-1} \quad (13)$$

The recombination rates derived from transient PL spectroscopy are plotted against reflux time in Figure 8. A gradual decrease of the nonradiative recombination rate is observed during the earlier reflux stage for both QD series, which suggests that the initial CdS shell coating (reflux time <2 h) is favorable for eliminating surface traps. During this stage, the radiative recombination rate also behaves in a rather similar way for $CdTe_{610}$ QDs (Figure 8a), giving rise to slightly enhanced PL QY. In contrast, that for $CdTe_{538}$ QDs (Figure 8b) presents a reverse tendency for the recombination rates, probably due to the effective elimination of surface traps present in greater proportion on smaller QDs. In consequence, the CdS coating more substantially increases the PL QY of $CdTe_{538}$ during this stage. Nevertheless, the maximum PL QYs achieved by $CdTe_{538}$ QDs (56% at 60 min of reflux) and $CdTe_{610}$ QDs (54% at 20 min of reflux) are rather comparable, suggesting that thin CdS shell coating can effectively increase the PL QY by eliminating the surface traps of the CdTe cores. Such a fluorescence enhancement effect was previously used to boost the PL QY to 85% at room temperature by Bao.[36] However, after the initial period of reflux, further growth of the CdS shell leads to nearly unchanged nonradiative recombination rates for both series

DOI: 10.1021/ja5127352
J. Am. Chem. Soc. 2015, 137, 2073–2084

QDs, but the radiative recombination rates is continuously decreased. In consequence, the PL QY for the CdTe/CdS QDs continued to decrease with further shell growth.

In principle, if the radiative recombination rate is decreased when forming a heterostructure, then it is necessary to decrease the nonradiative recombination rate more rapidly in order to obtain high PL QYs. The CdTe/CdS QDs reported herein presented substantially lower PL QYs than similarly structured QDs reported by Liu and co-workers,[37] obtained by aging magic-sized CdTe clusters (1.6 nm diameters) in aqueous solution containing Cd^{2+}−MPA at temperatures below 90 °C. From their reported data, i.e., 70% QY for 715 nm emitting QDs and the average lifetime of 82 ns for 700 nm emitting QDs, the radiative and nonradiative recombination rates of their CdTe/CdS QDs were roughly estimated to be around 0.85×10^7 s^{-1} and 0.37×10^7 s^{-1}, respectively, significantly different from 0.31×10^7 s^{-1} and 1.44×10^7 s^{-1} for the 685 nm emitting QDs reported herein (45 h data in Figure 8a). The prolonged radiative lifetime and shortened nonradiative lifetime, both unfavorable for the PL QY, are probably caused by the different reaction conditions (and shell growth rates). In the current case, the vigorous decomposition of GSH under reflux conditions largely accelerates the growth of the CdS shell, which inevitably introduces more traps in the CdS shell. According to the simulation results shown in Figure 7, the electron wave functions become largely located in the thickened CdS shell due to strain, contrasting to the situation in the absence of strain (Figure S9), thus the introduction of new defects in the shell may offset the removal of those at the initial core surface. This hypothesis, supported by the prolonged radiative lifetime and shortened nonradiative lifetime in comparison with the literature results as mentioned above, may serve to reconcile the differences in the PL QY behaviors of the CdTe/CdS core/shell QDs prepared with the different shell growth techniques.

CONCLUSIONS

In summary, a strain-modified effective mass approximation was proposed to model the optical behaviors of CdTe/CdS QDs formed by epitaxially coating CdTe QDs with a CdS shell through the thermally triggered release of sulfur from GSH. Because of the lattice mismatch, CdTe and CdS represent a typical strained system where CdTe core and CdS shell are subjected to compressive and tensile strains, respectively. To reveal the strain effect on the electronic structures, the pressure deformation potential was introduced to quantitatively predict the band alignment shifts of the system. Calculations revealed that the CBO rather than the VBO is more sensitive to the thickness of the CdS shell. In combination with these theoretical results, the electronic structure, carrier spatial distribution, and electron−hole wave function overlap were calculated by the extended EMA model and further compared with experimental results derived from both steady-state and time-resolved spectroscopy. Including strain and Coulomb interactions into the EMA model gives good agreement between the predicted and measured band edge transition energies. It was quantitatively revealed that the electron wave function progressively occupies the CdS shell region along with the shell growth, while the heavy hole remains largely confined in the CdTe core. Trends in the strain-modified EMA derived electron−hole wave function overlap, in QDs with different shell thicknesses, show excellent agreement with the experimentally derived oscillator strength. In conclusion, the strain-improved EMA model yields conclusive and constructive insights into band alignment shifts caused by strain, the consequent effects on carrier localization and recombination kinetics of core/shell nanocrystals, and the resulting impact on PL QY. Therefore, the current study could in large perspective be extended to unfold the intricate optical nature of lattice-mismatched core/shell QDs and even doped QDs, for rational design of advanced light-emitting nanomaterials.

ASSOCIATED CONTENT

Supporting Information

(1) Temporal evolutions of the PL peak position and the corresponding fwhm of $CdTe_{610}$ QDs in 12.58 mmol/L GSH aqueous solution at room temperature, (2) temporal evolutions of difference absorption spectra of $CdTe_{610}$ series QDs against reflux time, (3) the elemental composition evolutions of both $CdTe_{610}$ and $CdTe_{538}$ series QDs during reflux, (4) TEM and HRTEM images, and size distribution histograms of $CdTe_{538}$ series QDs against reflux time, (5) XRD patterns of $CdTe_{610}$ series QDs against reflux time, (6) fwhm and the corresponding normalized fwhm/peak maximum of $CdTe_{610}$ QDs in the 1.00 mmol/L GSH aqueous solution against reflux time, (7) time-resolved PL decay curves of $CdTe_{538}$ series QDs against reflux time, (8) detailed fitting processes for PL decay curves and tabulated fitting parameters, (9) tabulated deformation induced changes to conduction and valence band potentials together with CBO and VBO, (10) coulomb energy calculation for oppositely charged carrier pair, (11) radial conduction/valence potentials and wave functions calculated by leaving out strain-induced shifts, (12) calculated local field factor squared, f_{lf}^2, for $CdTe_{538}$ and $CdTe_{610}$ series QDs against reflux time. This material is available free of charge via the Internet at http://pubs.acs.org.

AUTHOR INFORMATION

Corresponding Author

gaomy@iccas.ac.cn

Author Contributions

‖Lihong Jing, Stephen V. Kershaw, and Tobias Kipp contributed equally to this work.

Notes

The authors declare no competing financial interest.

ACKNOWLEDGMENTS

The authors acknowledge funding from the National Basic Research Program of China (2011CB935800), the National Natural Science Foundation of China (21203210, 21321063, 81090271), and the Research Grants Council of the Hong Kong S.A.R., China (Project CityU 11302114)

REFERENCES

(1) Colvin, V. L.; Schlamp, M. C.; Alivisatos, A. P. *Nature* **1994**, *370*, 354.

(2) Anikeeva, P. O.; Halpert, J. E.; Bawendi, M. G.; Bulovic, V. *Nano Lett.* **2009**, *9*, 2532.

(3) Salter, C. L.; Stevenson, R. M.; Farrer, I.; Nicoll, C. A.; Ritchie, D. A.; Shields, A. J. *Nature* **2010**, *465*, 594.

(4) Nozik, A. J.; Beard, M. C.; Luther, J. M.; Law, M.; Ellingson, R. J.; Johnson, J. C. *Chem. Rev.* **2010**, *110*, 6873.

(5) Lan, X. Z.; Masala, S.; Sargent, E. H. *Nat. Mater.* **2014**, *13*, 233.

(6) Meinardi, F.; Colombo, A.; Velizhanin, K. A.; Simonutti, R.; Lorenzon, M.; Beverina, L.; Viswanatha, R.; Klimov, V. I.; Brovelli, S. *Nat. Photonics* **2014**, *8*, 392.

DOI: 10.1021/ja5127352
J. Am. Chem. Soc. 2015, 137, 2073−2084

(7) Resch-Genger, U.; Grabolle, M.; Cavaliere-Jaricot, S.; Nitschke, R.; Nann, T. *Nat. Methods* **2008**, *5*, 763.
(8) Cassette, E.; Helle, M.; Bezdetnaya, L.; Marchal, F.; Dubertret, B.; Pons, T. *Adv. Drug Delivery Rev.* **2013**, *65*, 719.
(9) Gao, J. H.; Zhang, W.; Huang, P. B.; Zhang, B.; Zhang, X. X.; Xu, B. *J. Am. Chem. Soc.* **2008**, *130*, 3710.
(10) Hines, M. A.; Guyot-Sionnest, P. *J. Phys. Chem.* **1996**, *100*, 468.
(11) Peng, X. G.; Schlamp, M. C.; Kadavanich, A. V.; Alivisatos, A. P. *J. Am. Chem. Soc.* **1997**, *119*, 7019.
(12) Dabbousi, B. O.; Rodriguez, V.; Heine, J. R.; Mattoussi, H.; Ober, R.; Jensen, K. F.; Bawendi, M. G. *J. Phys. Chem. B* **1997**, *101*, 9463.
(13) Tsay, J. M.; Pflughoefft, M.; Bentolila, L. A.; Weiss, S. *J. Am. Chem. Soc.* **2004**, *126*, 1926.
(14) Reiss, P.; Protière, M.; Li, L. *Small* **2009**, *5*, 154.
(15) Chen, O.; Zhao, J.; Chauhan, V. P.; Cui, J.; Wong, C.; Harris, D. K.; Wei, H.; Han, H. S.; Fukumura, D.; Jain, R. K.; Bawendi, M. G. *Nat. Mater.* **2013**, *12*, 445.
(16) Yang, Y. A.; Chen, O.; Angerhofer, A.; Cao, Y. C. *J. Am. Chem. Soc.* **2008**, *130*, 15649.
(17) Kim, S.; Fisher, B.; Eisler, H. J.; Bawendi, M. *J. Am. Chem. Soc.* **2003**, *125*, 11466.
(18) Smith, A. M.; Mohs, A. M.; Nie, S. *Nat. Nanotechnol.* **2009**, *4*, 56.
(19) Ivanov, S. A.; Piryatinski, A.; Nanda, J.; Tretiak, S.; Zavadil, K. R.; Wallace, W. O.; Werder, D.; Klimov, V. I. *J. Am. Chem. Soc.* **2007**, *129*, 11708.
(20) Balet, L. P.; Ivanov, S. A.; Piryatinski, A.; Achermann, M.; Klimov, V. I. *Nano Lett.* **2004**, *4*, 1485.
(21) Ma, X. D.; Mews, A.; Kipp, T. *J. Phys. Chem. C* **2013**, *117*, 16698.
(22) Tyagi, P.; Kambhampati, P. *J. Phys. Chem. C* **2012**, *116*, 8154.
(23) Soni, U.; Pal, A.; Singh, S.; Mittal, M.; Yadav, S.; Elangovan, R.; Sapra, S. *ACS Nano* **2014**, *8*, 113.
(24) Gupta, S.; Zhovtiuk, O.; Vaneski, A.; Lin, Y. C.; Chou, W. C.; Kershaw, S. V.; Rogach, A. L. *Part. Part. Syst. Charact.* **2013**, *30*, 346.
(25) Gupta, S.; Kershaw, S. V.; Rogach, A. L. *Adv. Mater.* **2013**, *25*, 6923.
(26) Smith, A. M.; Lane, L. A.; Nie, S. M. *Nat. Commun.* **2014**, *5*, 4506.
(27) Groeneveld, E.; Witteman, L.; Lefferts, M.; Ke, X. X.; Bals, S.; Van Tendeloo, G.; Donega, C. D. *ACS Nano* **2013**, *7*, 7913.
(28) Silva, A. C. A.; da Silva, S. W.; Morais, P. C.; Dantas, N. O. *ACS Nano* **2014**, *8*, 1913.
(29) Tang, Z. Y.; Wang, Y.; Shanbhag, S.; Kotov, N. A. *J. Am. Chem. Soc.* **2006**, *128*, 7036.
(30) Chen, X. B.; Lou, Y. B.; Samia, A. C.; Burda, C. *Nano Lett.* **2003**, *3*, 799.
(31) Baranov, A. V.; Rakovich, Y. P.; Donegan, J. F.; Perova, T. S.; Moore, R. A.; Talapin, D. V.; Rogach, A. L.; Masumoto, Y.; Nabiev, I. *Phys. Rev. B: Condens. Matter Mater. Phys.* **2003**, *68*, 165306.
(32) Dai, M. Q.; Zheng, W.; Huang, Z. W.; Yung, L.-Y. L. *J. Mater. Chem.* **2012**, *22*, 16336.
(33) Maltezopoulos, T.; Bolz, A.; Meyer, C.; Heyn, C.; Hansen, W.; Morgenstern, M.; Wiesendanger, R. *Phys. Rev. Lett.* **2003**, *91*, 196804.
(34) Diaconescu, B.; Padilha, L. A.; Nagpal, P.; Swartzentruber, B. S.; Klimov, V. I. *Phys. Rev. Lett.* **2013**, *110*, 127406.
(35) Banin, U.; Millo, O. *Annu. Rev. Phys. Chem.* **2003**, *54*, 465.
(36) Bao, H. B.; Gong, Y. J.; Li, Z.; Gao, M. Y. *Chem. Mater.* **2004**, *16*, 3853.
(37) Deng, Z. T.; Schulz, O.; Lin, S.; Ding, B. Q.; Liu, X. W.; Wei, X. X.; Ros, R.; Yan, H.; Liu, Y. *J. Am. Chem. Soc.* **2010**, *132*, 5592.
(38) Jing, L. H.; Yang, C. H.; Qiao, R. R.; Niu, M.; Du, M. H.; Wang, D. Y.; Gao, M. Y. *Chem. Mater.* **2010**, *22*, 420.
(39) Zeng, Q.; Kong, X.; Sun, Y.; Zhang, Y.; Tu, L.; Zhao, J.; Zhang, H. *J. Phys. Chem. C* **2008**, *112*, 8587.
(40) Gao, M. Y.; Kirstein, S.; Möhwald, H.; Rogach, A. L.; Kornowski, A.; Eychmüller, A.; Weller, H. *J. Phys. Chem. B* **1998**, *102*, 8360.
(41) Gaponik, N.; Talapin, D. V.; Rogach, A. L.; Hoppe, K.; Shevchenko, E. V.; Kornowski, A.; Eychmüller, A.; Weller, H. *J. Phys. Chem. B* **2002**, *106*, 7177.
(42) Shavel, A.; Gaponik, N.; Eychmüller, A. *J. Phys. Chem. B* **2006**, *110*, 19280.
(43) Yang, Y. H.; Wen, Z. K.; Dong, Y. P.; Gao, M. Y. *Small* **2006**, *2*, 898.
(44) Schooss, D.; Mews, A.; Eychmüller, A.; Weller, H. *Phys. Rev. B: Condens. Matter Mater. Phys.* **1994**, *49*, 17072.
(45) Nemchinov, A.; Kirsanova, M.; Hewa-Kasakarage, N. N.; Zamkov, M. *J. Phys. Chem. C* **2008**, *112*, 9301.
(46) Dinger, A.; Petillon, S.; Grün, M.; Hetterich, M.; Klingshirn, C. *Semicond. Sci. Technol.* **1999**, *14*, 595.
(47) Ithurria, S.; Tessier, M. D.; Mahler, B.; Lobo, R. P. S. M.; Dubertret, B.; Efros, A. L. *Nat. Mater.* **2011**, *10*, 936.
(48) Wei, S.-H.; Zunger, A. *Appl. Phys. Lett.* **1998**, *72*, 2011.
(49) Li, Y.-H.; Walsh, A.; Chen, S.; Yin, W.-J.; Yang, J.-H.; Li, J.; Da Silva, J. L. F.; Gong, X. G.; Wei, S.-H. *Appl. Phys. Lett.* **2009**, *94*, 212109.
(50) Li, Y. H.; Gong, X. G.; Wei, S. H. *Phys. Rev. B: Condens. Matter Mater. Phys.* **2006**, *73*, 245206.
(51) BenDaniel, D. J.; Duke, C. B. *Phys. Rev.* **1966**, *152*, 683.
(52) Leubner, S.; Schneider, R.; Dubavik, A.; Hatami, S.; Gaponik, N.; Resch-Genger, U.; Eychmüller, A. *J. Mater. Chem. C* **2014**, *2*, 5011.
(53) Dean, J. A. *Lange's Handbook of Chemistry*, 15th ed.; McGraw-Hill: New York, 1999.
(54) Tang, Z. Y.; Zhang, Z. L.; Wang, Y.; Glotzer, S. C.; Kotov, N. A. *Science* **2006**, *314*, 274.
(55) Haynes, W. M. *CRC Handbook of Chemistry and Physics*, 93rd ed.; CRC Press: Boca Raton, FL, 2012.
(56) Nonoguchi, Y.; Nakashima, T.; Kawai, T. *Small* **2009**, *5*, 2403.
(57) Cai, X. C.; Mirafzal, H.; Nguyen, K.; Leppert, V.; Kelley, D. F. *J. Phys. Chem. C* **2012**, *116*, 8118.
(58) Akinci, Ö.; Gürel, H. H.; Ünlü, H. *Thin Solid Films* **2009**, *517*, 2431.
(59) Allan, G.; Delerue, C. *Phys. Rev. B: Condens. Matter Mater. Phys.* **2012**, *86*, 165437.
(60) Kamal, J. S.; Omari, A.; Van Hoecke, K.; Zhao, Q.; Vantomme, A.; Vanhaecke, F.; Capek, R. K.; Hens, Z. *J. Phys. Chem. C* **2012**, *116*, 5049.
(61) Brus, L. E. *J. Chem. Phys.* **1984**, *80*, 4403.
(62) Keuleyan, S.; Kohler, J.; Guyot-Sionnest, P. *J. Phys. Chem. C* **2014**, *118*, 2749.

DOI: 10.1021/ja5127352
J. Am. Chem. Soc. 2015, 137, 2073−2084